Graphical abstract

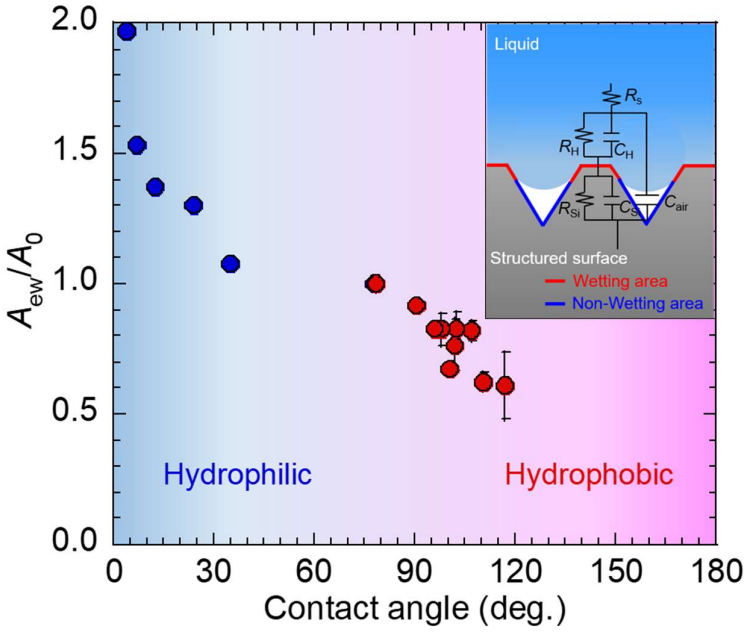

Measurement of effective wetting area at hydrophobic solid–liquid interface

Dejian Zhang[1], Satoko Takase[2], Gyoko Nagayama[1]*

[1]Department of Mechanical Engineering, Kyushu Institute of Technology, Sensui 1-1, Tobata, Kitakyushu, Fukuoka 804-8550, Japan

[2]Department of Chemical Engineering, Kyushu Institute of Technology, Sensui 1-1, Tobata, Kitakyushu, Fukuoka 804-8550, Japan

Corresponding Author:

Gyoko Nagayama

Email: nagayama.gyoko725@mail.kyutech.jp

ABSTRACT

Hypotheses: The effective wetting area, a parameter somewhat different from the apparent contact area at solid–liquid interfaces, plays a significant role in surface wettability. However, determination of the effective wetting area for hydrophobic surfaces remains an open question. Therefore, in the present study, we developed an electrochemical impedance method to evaluate the effective wetting area at a hydrophobic solid–liquid interface.

Experiments: Patterned Si surfaces were prepared using the anisotropic wet etching method, and the water contact angle and electrochemical impedance were measured experimentally. The effective wetting area at the solid–liquid interface was examined based on the wettability and impedance results.

Findings: The electrochemical impedance for the patterned Si surfaces increased with increasing surface hydrophobicity, whereas the effective wetting area decreased. The intermediate wetting state (i.e. partial wetting model) was confirmed at the patterned Si surfaces, and the effective wetting area was theoretically estimated. The effective wetting area predicted from the electrochemical impedance agreed well with that predicted from the partial wetting model, thereby demonstrating the validity of the electrochemical impedance method for evaluating the effective wetting area at the hydrophobic solid–liquid interface.

Keywords: Effective wetting area, Hydrophobic surface, Contact angle, Electrochemical impedance, Partial wetting model

1. Introduction

Surface wettability is a common and important phenomenon with various practical applications in science and technology [1–6]. Generally, solid surfaces with water contact angles (WCAs, i.e. θ) greater than 90^{o} are considered hydrophobic, depending on the physical topography and chemical composition of the surface. In recent decades, theoretical studies on hydrophobic mechanisms [7–10] and experimental investigations regarding hydrophobic wetting behavior [11–13] have attracted considerable research attention. Considering the influence of the physical topography on surface wettability, Wenzel modified Young's equation by introducing the surface area increment ratio, r_{w}, and proposed a fully wetted state [14]. Cassie and Baxter subsequently introduced the composite interface, i.e., liquid floating over asperities at the structured surface in a non-wetted state [15]. However, pure Wenzel or Cassie–Baxter wetting states rarely occur in practice [16–18]. Experimental WCAs can be larger or smaller than those deduced from the Wenzel and Cassie–Baxter models [19,20]. In our previous study, we developed a partial wetting model to describe the general solid–liquid contact mode at a solid–liquid interface [21].

The characterization of surface wettability usually focuses on the contact angle or contact angle hysteresis. However, in most applications of advanced materials, it is also essential to clarify the wetting state and hence the effective wetting area, i.e., the actual solid–liquid contact area at the surface or interface of colloidal materials and nanomaterials. Moreover, the effective wetting area is the original parameter linking wetting phenomena to thermal and electrical transport at the solid–liquid interface [22,23]. Interfacial resistance, i.e., thermal resistance or electrochemical impedance, is generally

inversely proportional to the wetting area, with larger contact areas implying a smaller interfacial resistance [24].

In our previous paper, we defined the effective wetting ratio, f, as a dominant parameter for analyzing surface wettability [21]. The effective wetting ratio ranges from 0, for the non-wetted Cassie–Baxter state, to 1, for the fully wetted Wenzel state. However, direct measurement of the solid–liquid contact area is extremely difficult. Hence, to overcome this limitation, various optical techniques including confocal microscopy [25–27], interference microscopy [28,29], and beam reflection methods [30,31] have been proposed to visualize the wetting state inside nano/microstructures. These approaches offer favorable conditions to further investigate the wetting behaviors inside structures. However, none of these techniques provide information regarding the effective wetting area, and optical methods are limited to transparent materials. Non-optical approaches for determining liquid penetration within structures include quartz crystal microbalance techniques [32], in situ x-ray diffraction [33], acoustic tracking [34–36], and electrochemical impedance [37,38]. Recently, we evaluated the effective wetting area at a hydrophilic solid–liquid interface by applying wetting states for electrochemical impedance analysis [38]. We noted that the impedance modulus decreases as the WCA decreases, confirming the dependence of WCA on the effective wetting area at the solid–liquid interface. However, determination of the effective wetting area for hydrophobic surfaces remains an open question and the accuracy of electrochemical impedance method needs further verification in this regard.

In the present study, we theoretically and experimentally investigated the effective wetting area at the solid–liquid interface for hydrophobic surfaces. We applied regular

structured surfaces for further deepened theoretical discussions related to Ref. [21]. We measured the electrochemical impedance of patterned Si surfaces and estimated the effective wetting area experimentally based on the electrochemical impedance analysis. In addition, we measured the WCAs on the patterned Si surfaces and calculated the effective wetting area theoretically based on the partial wetting model. The effective wetting areas predicted from the experimental and theoretical results were compared to verify the validity of the electrochemical impedance method. To the best of our knowledge, ours is the first efficient method to estimate the effective wetting area at a hydrophobic solid–liquid interface, which is challenging to measure directly through experiments.

2. Materials and methods

2.1. Sample preparation and characterization

Experiments were performed using N-type (100) Si wafers with a 350-μm thickness. Substrates measuring 15 × 15 mm were cut from the Si wafers. Before fabrication, the Si substrates were ultrasonically cleaned using acetone and isopropyl alcohol sequentially for 10 min to remove dirt and other possible contaminants and subsequently rinsed in deionized (DI) water. The cleaned substrates were dipped in a 1% buffered hydrofluoric acid solution (BHF) for 1 min to remove the natural SiO_2 layer and then cleaned in DI water. To obtain patterned structures on the Si surfaces, anisotropic wet etching (used in conventional microelectromechanical system fabrication technology) was employed, resulting in uniform micropores over a 10 × 10 mm^2 area; the detailed fabrication process

is illustrated in Fig. 1. The surface morphologies of patterned Si samples were analyzed using a scanning electron microscope (SEM, JSM-6701 FONO, JEOL).

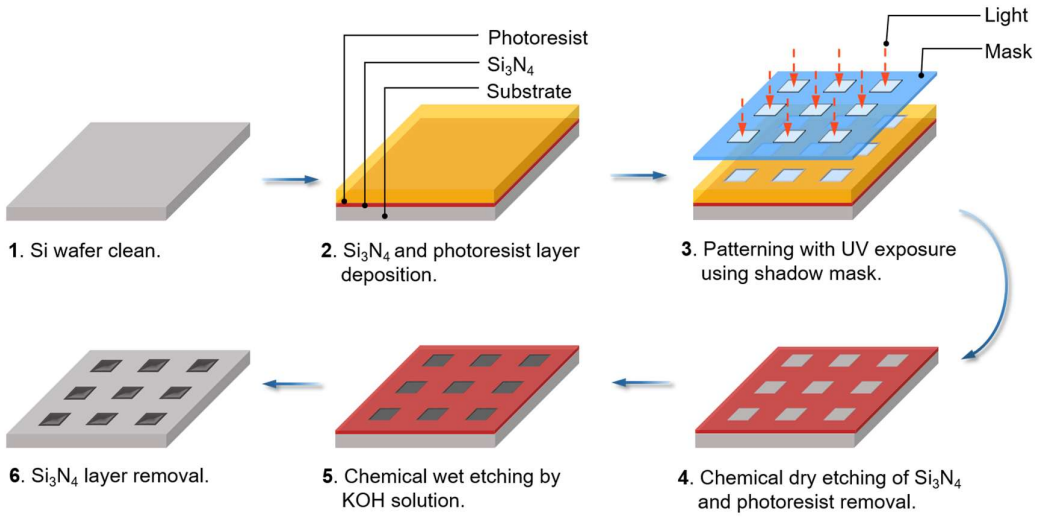

Fig. 1. Schematic illustration of the procedure employed to prepare patterned Si surfaces.

2.2. Contact angle measurement

The wetting behavior was investigated at ambient conditions (25℃, 40% RH). A measurement cell (Fig. s1) was used to cover the droplet and the substrate to prevent contaminant adsorption during measurement. The measurement cell was made by transparent organic glass with the size of 10 cm × 10 cm × 10 cm. A digital temperature-humidity sensor was put inside the cell to monitor the local temperature and humidity. Four microliter (4 μL) pure water (Wako, LC/MS 214-01301) droplets were dropped carefully onto the surface. The side views of droplets were obtained using a digital microscope (Keyence VHX-200) and the contact angle measurements were performed using the $\theta/2$ method [39].

Before measuring the contact angles for the structured Si surfaces, each sample was immersed in acetone and the BHF solution to remove any contaminants and natural SiO_2 layers, and then repeatedly rinsed under pure water. The WCA for the unetched areas of all the samples was $\theta_Y = 78.6 \pm 1.0°$, thus confirming surface composition uniformity (Fig. s2). The average WCA was determined by measuring the angle on the same surface at three positions, and the standard deviation was used to evaluate the error.

2.3. Electrochemical impedance measurement

Electrochemical measurements were performed using the same substrates to the wettability measurements but in a separate experimental system (Fig. s3). An electrochemical workstation (Biologic-SP-200) was operated with a three-electrode system in a 3.5 wt% NaCl solution at ambient temperature. The measurement system was placed in a Faraday cage to shield the interference of external electric field. The system comprised Si samples with a 1 cm^2 (1 × 1 mm) exposed surface area as the working electrode, a platinum foil with a 4 cm^2 (10 × 20 mm × 2 sides) as the counter electrode, and a silver/silver chloride electrode as the reference electrode. The electrodes were worked in a glass cell with polytetrafluoroethylene (PTFE) caps. A nature rubber sealing ring is used to prevent the penetration of the electrolyte from the cell to the outside. A supporting Al plate is attached to the working electrode to make electrical contact. The measurement was conducted by immersing the substrate vertically in a bulk liquid electrolyte. Electrochemical impedance spectroscopy (EIS) was carried out with a 10 mV sinusoidal signal in a frequency range from 1 MHz to 100 mHz. Six values were collected per decade in logarithmic spacing, with every measurement repeated twice and averaged for each frequency. It should be noted that the electrical field is weak and the effect of

electrowetting is almost negligible. Before performing electrochemical measurements, the Si samples were immersed in the electrolyte till the variation of the open circuit voltage was less than 2 mV within 5 min. The EIS data were modeled using equivalent electrical circuits (EECs), and curve fitting was performed using the ZSimpWin software [40].

The wettability of pure water on Si surfaces showed a slight difference from that of the electrolyte. The contact angle discrepancies between pure water and the electrolyte were within the measurement error range, as shown in Fig. s4 and Table s1. Thus, we used pure water for all the subsequent wettability analyses.

3. Results and discussion

3.1. Surface morphology and wettability

Uniform square-patterned structures were fabricated on the Si substrates over a 1 cm^2 area. The sizes of the square orifices of the pores, a, ranged from 3 to 12 μm, and the spacing between the pores, b, ranged from 2 to 7 μm. Table s2 summarizes the selected geometrical parameters used to define the microstructures evaluated in this work. Figure 2a shows typical images of the fabricated patterned Si surfaces, with square pores measuring 5 × 5 μm in a regular array on the top surface. As shown in Fig. 2b, the cross-section of the square pores is triangular in shape owing to the anisotropic wet etching process used for preparing the patterned structures. Therefore, the pore height, h, was determined by the square orifice and the specific angle, α (54.74°), between the Si (111) and (100) crystal planes.

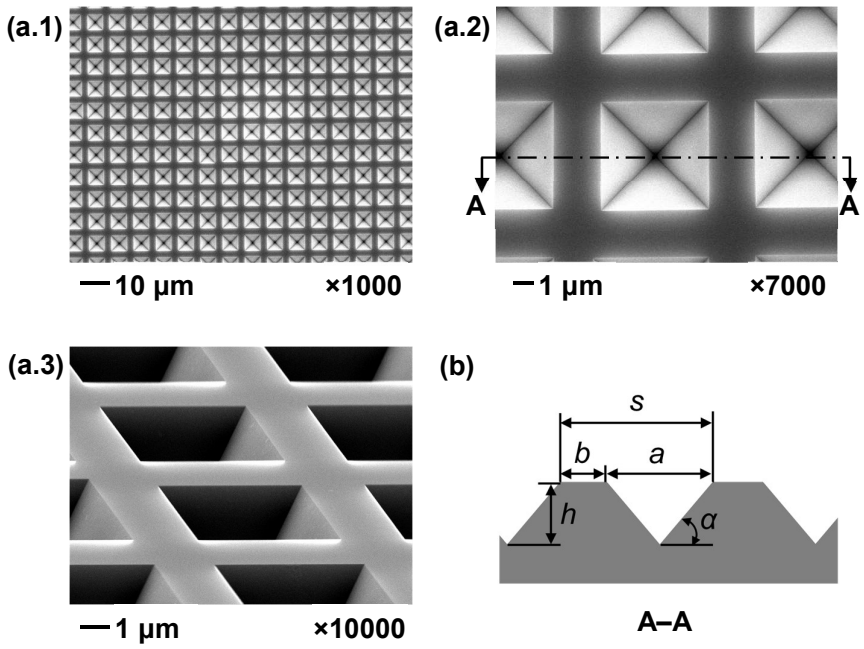

Fig. 2. Patterned Si surface (a) typical SEM images with a = 5 μm and b = 3 μm; (b) cross-sectional view (A–A) with detailed parameters a, b, h, s, and α.

The solid fraction, Φ, and surface area increment ratio, r_w, can be expressed, respectively, as

$$\Phi = \frac{s^2 - a^2}{s^2} \tag{1}$$

and

$$r_w = \frac{s^2 - a^2 + a^2 / \cos\alpha}{s^2}. \tag{2}$$

Thus, the modified Wenzel, Cassie–Baxter, and partial wetting models for the triangular patterned Si surface are as follow:

$$\cos\theta_{\mathrm{w}} = r_{\mathrm{w}}\cos\theta_{\mathrm{Y}} = \frac{s^2 - a^2 + a^2/\cos\alpha}{s^2}\cos\theta_{\mathrm{Y}}, \tag{3}$$

$$\cos\theta_{\mathrm{C}} = \Phi\cos\theta_{\mathrm{Y}} + (1-\Phi)\cos 180^{\circ} = \frac{s^2 - a^2}{s^2}\cos\theta_{\mathrm{Y}} + \frac{a^2}{s^2}\cos 180^{\circ}, \tag{4}$$

and

$$\begin{aligned}\cos\theta_{\mathrm{P}} &= \left[\Phi + (r_{\mathrm{w}} - \Phi) f\right]\cos\theta_{\mathrm{Y}} + (1-\Phi)(1-f)\cos 180^{\circ} \\ &= \frac{(s^2 - a^2) + (a^2/\cos\alpha) f}{s^2}\cos\theta_{\mathrm{Y}} + \frac{a^2(1-f)}{s^2}\cos 180^{\circ},\end{aligned} \tag{5}$$

respectively, where θ_{Y}, θ_{W}, θ_{C}, and θ_{P} are the contact angles for the Young, Wenzel, Cassie–Baxter, and partial wetting models, respectively [14,15,21,41]. The effective wetting ratio f is the proportion of solid–liquid contact area to the apparent area inside of structures, which can be expressed as $f = 1 - \Phi^{\mathrm{D-2}}$ empirically [21]. The fractal dimension D is obtained based on the box-counting method with the aid of fractal analysis software [42,43]. The mean D for patterned Si surfaces was 2.24 (see Table s3 in the supporting materials).

Figure 3a shows the side views of water droplets on the prepared Si surfaces and the static equilibrium WCAs are summarized in Table s2. All the WCAs presented are means calculated from three measurements. The WCA was 78.6 ± 1.0° for the flat Si surface, which was ascribed solely to the surface chemical composition. Compared to the flat surface, larger values were obtained for the patterned Si surfaces, varying from 90.6 ± 1.2° to 116.8 ± 2.3°. These results show that the patterned microscale porous structures

enhanced surface hydrophobicity, indicating the effect of surface physical morphology on wettability.

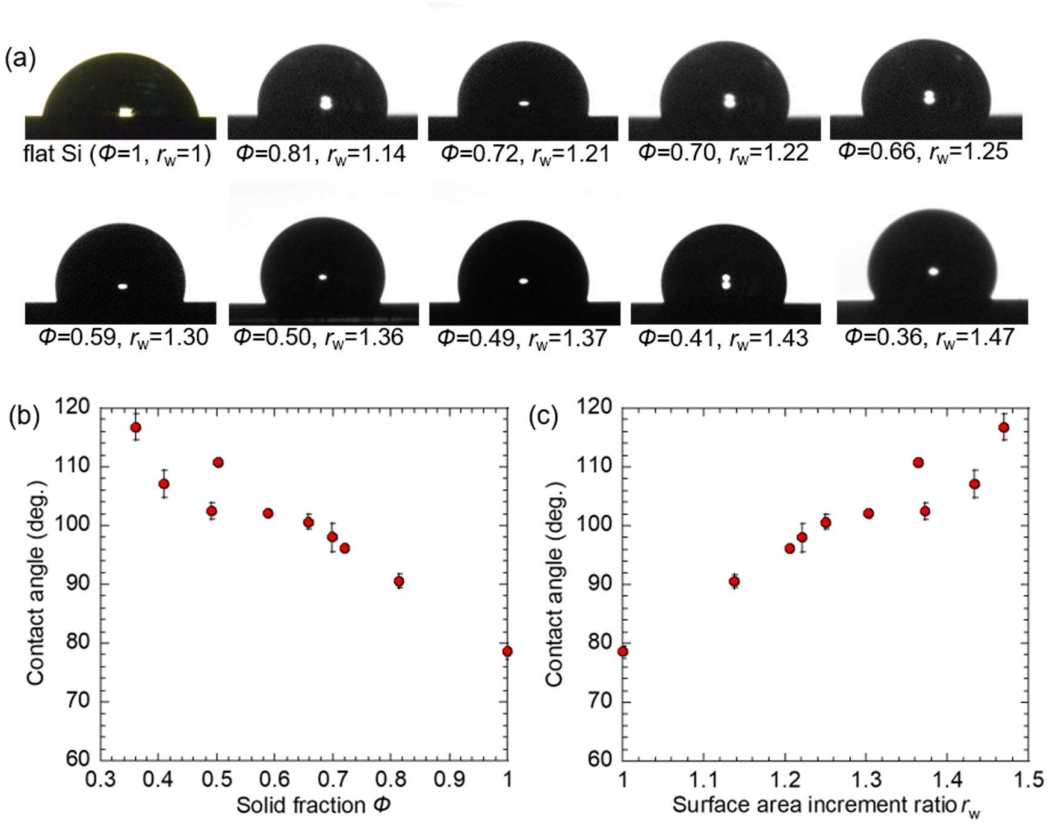

Fig. 3. Droplets upon patterned Si surfaces: (a) microscope images and experimental WCAs with respect to (b) solid fraction Φ and (c) surface area increment ratio r_w.

The dependence of wettability on surface morphology was confirmed by examining the influence of Φ and r_w on the WCA. As illustrated in Fig. 3b, the WCA decreased with increasing Φ. The largest WCA was obtained for the patterned Si surface with Φ = 0.36, and the smallest WCA for that with Φ = 0.81. Figure 3c shows that the correlation between the WCA and r_w is the opposite of that between the WCA and Φ; the WCA increases with increasing r_w. As Φ and r_w are dominant factors for surface wettability

with opposite influences, we used Φ as the typical physical factor for the subsequent wettability analyses.

Figure 4 compares the experimentally measured WCAs and theoretical results predicted from the Wenzel, Cassie–Baxter, and partial wetting models. It shows the theoretical WCA results calculated from Eqs. 3–5, with diverse trends obtained for the different models. We observed that the experimental WCAs differed significantly from those calculated using the Wenzel model for the typical solid fraction range of $0.36 < \Phi < 1$ but showed tendencies similar to the WCAs determined using the Cassie–Baxter and partial wetting models. However, the experimental WCAs were more consistent with the theoretical predictions made from the partial wetting model compared to those obtained from the Cassie–Baxter model, implying that the contact mode at the solid–liquid interface of the patterned Si surface is closer to the partial wetting model.

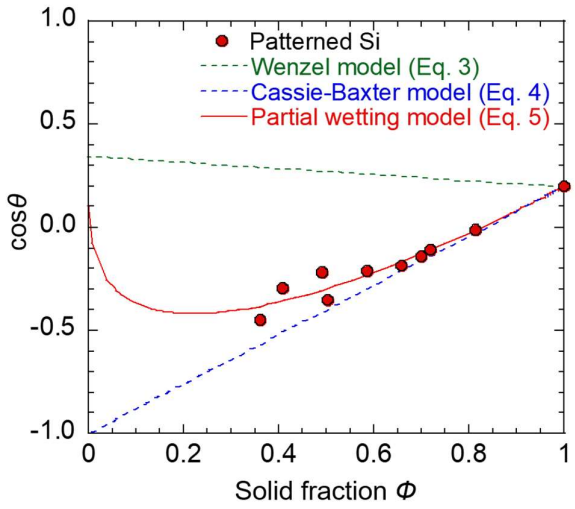

Fig. 4. Comparisons between experimental WCA results and those obtained from wetting models for patterned Si surfaces.

3.2. Electrochemical impedance analysis

Electrochemical properties of the patterned Si surfaces were analyzed using EIS and EEC. The typical Nyquist plots and the corresponding fitted curves for Si surfaces with WCAs of 78.6, 90.6, 102.1, and 116.8° are illustrated in Fig. 5. The semicircles in the Nyquist plots indicate the effect of double-layer capacitance, where larger arcs mean larger impedance. We can observe that the capacitive arc diameters for the patterned Si surfaces are larger than that for the flat surface. Moreover, the samples with larger WCAs have larger impedances, indicating that impedance is directly proportional to surface hydrophobicity. In addition, the Nyquist plots presented in Fig. s6 for the other patterned Si surfaces show tendencies similar to the results plotted in Fig. 5.

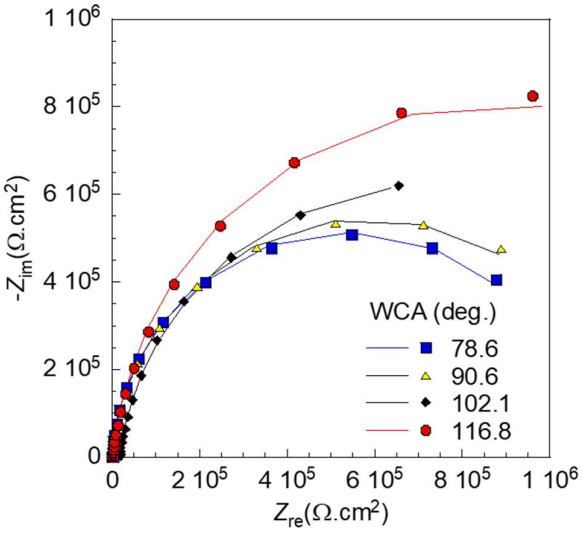

Fig. 5. Typical Nyquist plots of Si surfaces with WCAs of 78.6, 90.6, 102.1, and 116.8° in 3.5 wt% NaCl solution. Symbols represent the measured results and lines are the corresponding fitted curves.

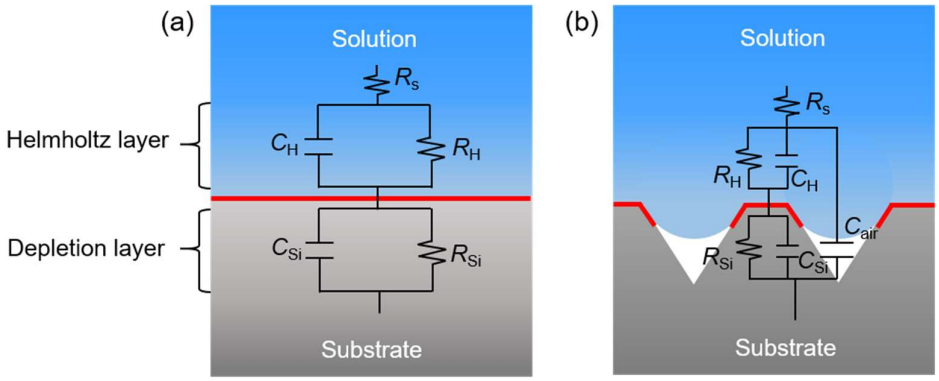

Fig. 6. Schematics of solid–liquid interface and EECs for Nyquist fitting on (a) flat and (b) patterned Si surfaces.

To evaluate the electrochemical parameters from the measured impedance spectra, schematics of the solid–liquid interface and two-time constant EECs were used to fit the obtained Nyquist results, as shown in Fig. 6. Since the electrochemical behavior at the semiconductor-electrolyte interface is affected by electrolyte, the Helmholtz layer and the depletion layer [44, 45], we used R_s, R_H, and R_{Si} to denote the solution resistance, the transfer resistance of electrons and ions through the Helmholtz layer and the depletion layer, respectively [44]. As defects and inhomogeneities cannot be avoided on the electrode surface, capacitors often do not exhibit ideal capacitive behavior. Therefore, we applied the constant phase element (CPE) to determine the non-ideal frequency-dependent properties of the Helmholtz layer capacitance C_H and the depletion layer capacitance C_{Si}. The impedance of the CPE is defined by the CPE constant and CPE index, which is described as follows:

$$Z_{CPE} = \frac{1}{Q(j\omega)^n}, \quad (6)$$

where Q is the CPE magnitude, j is the imaginary root, ω is the angular frequency, and n is a deviation parameter regarding the phase shift.

In section 3.1, we have confirmed the intermediate wetting state at the patterned Si surfaces; namely, the non-wetting area exists at the solid–liquid interface. To examine the role of the non-wetting area in the EEC, a circuit with capacitive element, air capacitance C_{air}, was added as a parallel component for the EEC of the patterned Si surfaces, as shown in Fig. 6b. As the electronic and ionic conductivities are almost zero for air, ions and electrons cannot move through the non-wetted area. Thus, electrochemical impedance is dominated by the solid–liquid contact area (red parts in Fig. 6). Analysis of the Nyquist plots showed that the impedance of the patterned Si surfaces is larger than that of the flat Si surface, indicating that the presence of non-wetting areas results in a smaller contact area between the substrate and electrolyte.

The obtained electrochemical parameters per unit apparent area, including R_s, R_H, R_{Si}, CPE_H *and* CPE_{Si}, are listed in Table 1. Generally, impedance in low-frequency regions more clearly represents electrochemical properties and better clarifies the effective wetting area on structured surfaces [46–48]. Compared to the values of R_{Si} and R_H, that of R_s is small enough to be neglected. Based on the EEC shown in Fig. 6, the interfacial impedance Z at low frequencies is equal to the sum of R_H and R_{Si}. We noted that the Z values increased with increasing WCAs, from 1.07×10^6 Ω.cm^2 for the flat surface (θ = 78.6°) to 1.76×10^6 Ω.cm^2 for the patterned Si surfaces with Φ = 0.36 (θ = 116.8°), which correspond well with the Nyquist plots. The correlation between the impedance and WCA can be explained by analyzing the effective wetting area. For a constant-volume droplet on the solid surface, the effective wetting area is inversely proportional to the contact

angle. Thus, a larger WCA results in a smaller solid–liquid contact area, thereby increasing Z.

Table 1. Measured electrochemical parameters for Si samples in 3.5 wt% NaCl solution.

WCA (deg.)	R_s ($\Omega.cm^2$)	CPE_{Si}		CPE_H		R_{Si} ($\Omega.cm^2$)	R_H ($\Omega.cm^2$)
		Q (Ω^{-1} s^n/cm^2)	n	Q (Ω^{-1} s^n/cm^2)	n		
90.6	36	9.76×10^{-10}	0.95	5.00×10^{-7}	0.96	6.24×10^{3}	1.17×10^{6}
98.0	63	5.21×10^{-10}	0.93	4.33×10^{-7}	0.93	3.25×10^{3}	1.30×10^{6}
110.7	15	8.44×10^{-10}	0.93	5.55×10^{-7}	0.99	2.04×10^{3}	1.72×10^{6}
96.1	38	5.02×10^{-9}	0.93	4.95×10^{-7}	0.83	3.27×10^{3}	1.30×10^{6}
102.1	10	7.43×10^{-10}	0.97	8.72×10^{-7}	0.92	1.78×10^{4}	1.40×10^{6}
107.1	30	2.85×10^{-9}	0.90	8.92×10^{-7}	0.95	7.22×10^{3}	1.30×10^{6}
100.6	23	4.39×10^{-9}	0.93	3.85×10^{-7}	0.84	3.49×10^{3}	1.60×10^{6}
102.6	51	2.79×10^{-8}	0.75	1.09×10^{-6}	0.93	8.80×10^{3}	1.29×10^{6}
116.8	37	6.44×10^{-9}	0.87	5.37×10^{-7}	0.94	2.82×10^{3}	1.76×10^{6}
78.6	22	5.47×10^{-10}	1.00	4.57×10^{-7}	0.97	2.03×10^{3}	1.07×10^{6}

3.3 Effective wetting area estimation based on electrochemical impedance

Since the impedance for specific materials per unit solid–liquid contact area is constant, the effective wetting area, A_{ew}, can be estimated as [38]

$$A_{ew} = \frac{|Z_0|}{|Z|} A_0, \tag{7}$$

where A_0 is the apparent area of the flat Si surface, and Z_0 and Z are the measured impedances for the flat and patterned Si surfaces, respectively.

The area ratios of the effective wetting areas on structured surfaces to those of the corresponding flat surfaces, A_{ew}/A_0, calculated from the experimental impedance results are presented as functions of the WCAs in Fig. 7. The obtained A_{ew}/A_0 values decreased with increasing WCAs. The minimum A_{ew}/A_0 value of 0.610 was obtained for the patterned Si surface ($\Phi = 0.36$; $\theta = 116.8°$), and the maximum value of 1.000 was obtained for the flat Si surface ($\Phi = 1$; $\theta = 78.6°$). The blue closed circles shown in Fig. 7 represent the A_{ew}/A_0 values for the hydrophilic Al surfaces taken from our previous work [38]. Despite the different materials and wettabilities, the correlation between the A_{ew}/A_0 and WCA for the hydrophobic Si surfaces (present study) matches reasonably well with that for the hydrophilic surfaces.

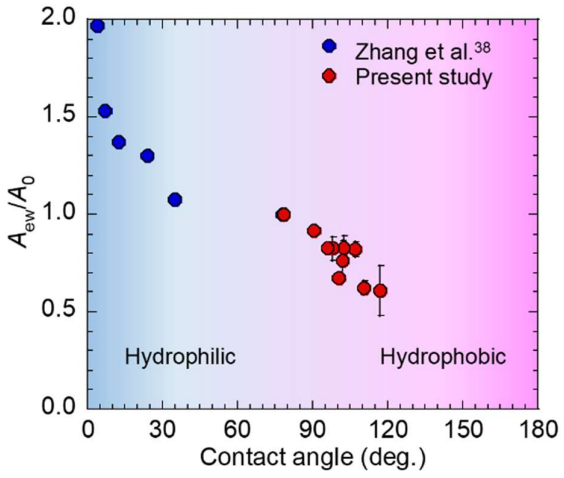

Fig. 7. Effective wetting area ratios evaluated based on experimental electrochemical impedance results for both hydrophilic and hydrophobic surfaces.

3.3. Effective wetting area estimation based on experimental WCAs and partial wetting model

Based on the partial wetting model (Eq. 5), the effective wetting ratio, f, can be calculated by substituting the measured WCAs, θ_Y and θ_P, and structural parameters Φ and r_w.

$$f = \frac{\cos\theta_P - \Phi\cos\theta_Y + (1-\Phi)}{(r_w - \Phi)\cos\theta_Y + (1-\Phi)} \quad (8)$$

The red closed circles shown in Fig. 8 represent the f values calculated using Eq. 8 with the Φ ranging from 0.36 to 1. The black open circles indicate the f estimated in a similar manner in another study [21] for patterned Si surfaces with Φ = 0–0.4. We found that the estimated f decreased with increasing Φ over a wide region. The solid line represents an emperical equation for f proposed earlier [21]. Although slightly data scattering occurs, the estimated results based on experimental measurements agree well with the values determined using the empirical equation.

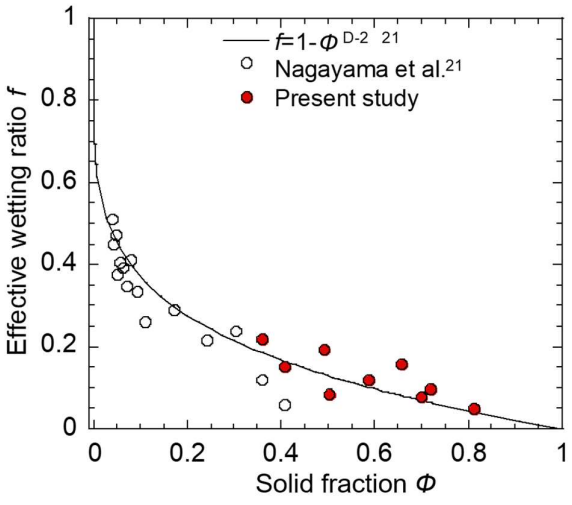

Fig. 8. Effective wetting ratio f as a function of solid fraction Φ: comparisons between the present study and a previous one [21].

Table 2. Effective wetting area evaluated from wettability (Eq. 9) and electrochemical impedance results (Eq. 7).

Solid fraction Φ	WCA (deg.)	A_{ew}/A_0 (Eq. 9)	A_{ew}/A_0 (Eq. 7)
0.81	90.6 ± 1.2	0.834 ± 0.011	0.914 ± 0.040
0.70	98.0 ± 2.3	0.729 ± 0.017	0.825 ± 0.060
0.50	110.7 ± 0.6	0.559 ± 0.003	0.624 ± 0.027
0.72	96.1 ± 0.1	0.761 ± 0.001	0.827 ± 0.126
0.59	102.1 ± 0.4	0.699 ± 0.003	0.764 ± 0.061
0.41	107.1 ± 2.3	0.688 ± 0.015	0.821 ± 0.010
0.66	100.6 ± 1.3	0.693 ± 0.009	0.672 ± 0.100
0.49	102.6 ± 1.3	0.742 ± 0.009	0.828 ± 0.037
0.36	116.8 ± 2.3	0.512 ± 0.010	0.610 ± 0.023
1.00 (flat)	78.6 ± 1.0	1.000 ± 0.013	1.000 ± 0.029

In the partial wetting model, A_{ew}/A_0 is equal to $\Phi+\left(r_w-\Phi\right)f$ and thus it can be expressed as

$$A_{ew}/A_0=\Phi+\left(r_w-\Phi\right)f=\Phi+\left(r_w-\Phi\right)\frac{\cos\theta_P-\Phi\cos\theta_Y+\left(1-\Phi\right)}{\left(r_w-\Phi\right)\cos\theta_Y+\left(1-\Phi\right)}, \quad (9)$$

where the maximum A_{ew}/A_0 of 1 was obtained for the flat surface with $\Phi = r_w = 1$. The A_{ew}/A_0 obtained from Eq. 9 are summarized in Table 2. It is clear that surfaces with larger WCAs have smaller A_{ew}/A_0, and the minimum A_{ew}/A_0 of 0.610 is for the patterned surface

with the WCA of 116.8°. Table 2 also shows the A_{ew}/A_0 based on the electrochemical impedance results explained in section 3.3. For the same A_0, the A_{ew} estimated from Eq. 9 agrees well with that calculated from Eq. 7.

The A_{ew}/A_0 calculated from the wettability and impedance results are compared in Fig. 9. We can clearly see that the ratios obtained from both the wettability and impedance results show a downward trend with increasing WCAs; i.e., the effective wetting area is inversely proportional to surface hydrophobicity. Additionally, the A_{ew}/A_0 obtained from the impedance results are slightly larger than those calculated from the wettability results. This difference occurred because impedance measurements were performed by immersing the Si surfaces in the electrolyte, while the wettability measurements were performed under atmosphere. In our impedance measurements, additional hydrostatic pressure of 147 Pa approximately was imposed to the Si surface, resulting in a larger effective wetting area at the solid–liquid interface. Hence, larger area ratios were obtained from the impedance measurements than those from the wettability measurements. However, despite some minor deviations, the effective wetting areas calculated from the impedance and wettability measurements corresponded well.

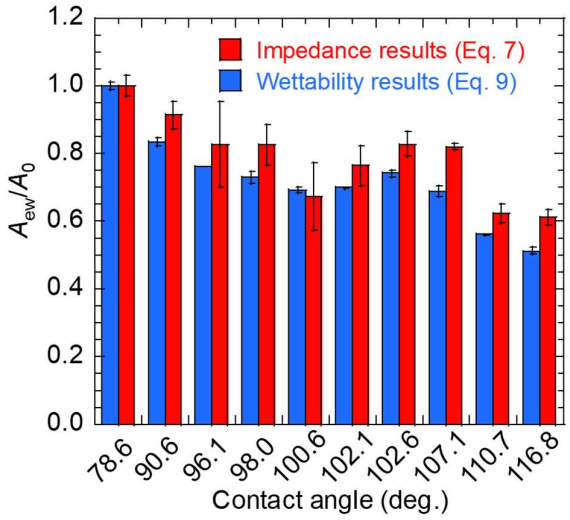

Fig. 9. Effective wetting area ratio evaluated from impedance (Eq. 7) and wettability results (Eq. 9).

Figure 10 compares the A_{ew}/A_0 determined from the experiments and theoretical wetting models. The A_{ew}/A_0 calculated from the Wenzel model decreases with increasing Φ, from 1.47 at Φ = 0.36 to 1 at Φ = 1. The opposite tendency can be observed for the A_{ew}/A_0 from the Cassie–Baxter and partial wetting models; the A_{ew}/A_0 increase with increasing Φ in the measured solid fraction range.

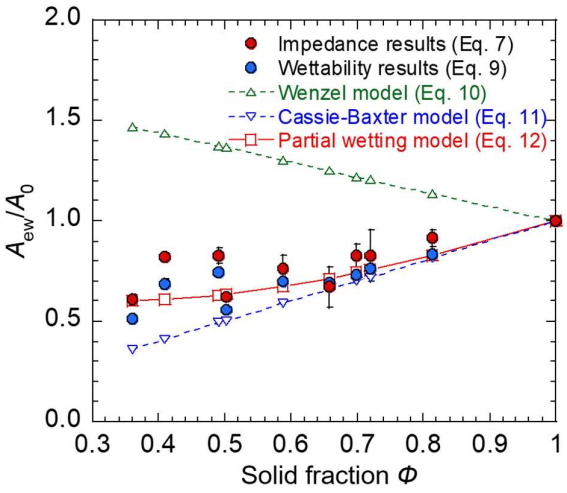

Fig. 10. Comparisons of A_{ew}/A_0 obtained from experiments and theoretical models.

The effective wetting areas determined from the Wenzel, Cassie–Baxter, and partial wetting models can be expressed, respectively, in terms of the Si surface structural parameters as

$$A_{\text{ew-W}} = A_0 \times r_w = A_0 \frac{s^2 - a^2 + a^2/\cos\alpha}{s^2}, \tag{10}$$

$$A_{\text{ew-C}} = A_0 \times \Phi = A_0 \frac{s^2 - a^2}{s^2} \text{ and} \tag{11}$$

$$A_{\text{ew-P}} = A_0 \times \left[\Phi + (r_w - \Phi) f\right] = A_0 \frac{(s^2 - a^2) + (a^2/\cos\alpha) f}{s^2}. \tag{12}$$

For a given Φ, the area ratio predicted from the partial wetting model (Eq. 12) is larger than that obtained from the Cassie–Baxter model (Eq. 11), implying that wetting area $A_{\text{ew-P}}$ is larger than $A_{\text{ew-C}}$. These area ratios are similar to those in Fig. 4, with the A_{ew}/A_0 obtained from the experimental results (blue and red closed circles) agreeing reasonably

with those calculated from the partial wetting model (red open squares) but deviating from the Wenzel and Cassie–Baxter models. This observation further confirmed the intermediate wetting state at the patterned Si surfaces. Additionally, we verified the validity and feasibility of the electrochemical impedance method for estimating the effective wetting area. Thus, the proposed approach offers an efficient method to estimate the effective wetting area at hydrophobic solid–liquid interfaces.

However, the electrochemical impedance method is difficult to be applied to the dielectric materials. Besides the limitations in common with the conventional electrochemical impedance measurement, the impedance measurements were limited to be performed in a separate experimental system to the wettability measurements. The pressure difference at solid–liquid interface between the impedance and wettability measurements will cause the deviations of the estimated effective wetting areas. Simultaneous measurements of the impedance and the wettability are necessary to overcome this limitation; however, an electrochemical impedance system for a single fine droplet on a substrate is still a challenging work.

4. Conclusions

We developed an electrochemical impedance method for determining the effective wetting area at solid–liquid interfaces experimentally and theoretically. For this purpose, we fabricated patterned Si surfaces and measured the WCAs. In addition, we found that the electrochemical impedance increased with increasing surface hydrophobicity, whereas the effective wetting area decreased. The correlation between the A_{ew}/A_0 and WCA for the hydrophobic Si surfaces matches reasonably well with that for hydrophilic

surfaces [38]. The effective wetting area was further theoretically estimated based on the WCAs and the partial wetting model including a novel concept of the intermediate wetting state [21]. We verified that the experimentally determined effective wetting areas agreed well with the theoretically calculated ones; the areas decreased with increasing WCAs. In conclusion, the proposed electrochemical impedance method offers improved efficiency and accuracy for estimating the effective wetting area at the solid–liquid interface.

The solid–liquid interfaces at the patterned Si surfaces fabricated in this study were hydrophobic, showing the intermediate wetting state between the Wenzel and Cassie–Baxter states. In such circumstances, there is no guarantee that the effective wetting area, i.e., the real solid–liquid contact area, is the same as the apparent solid–liquid contact area on structured surfaces. To accurately estimate the effective wetting area, understanding the intermediate wetting state is absolutely essential for the actual solid–liquid contact area at the surface or interface of colloidal materials and nanomaterials.

Existing optical [25–31] techniques are limited to the transparent materials, and non-optical [32–37] techniques are mainly focus on the wetting state monitoring without accurate quantitative estimates of the effective wetting area. To the best of our knowledge, our method is the first efficient means to estimate the effective wetting area at hydrophobic solid–liquid interfaces, which remains difficult to measure directly through experiments.

The proposed electrochemical impedance method for measuring the effective wetting area was verified at the solid–liquid interface immersed in a liquid, which may differ from

that at the interface beneath a droplet. Further development of the electrochemical impedance method on microelectrode array chips are under way to determine the effective wetting area of a single fine droplet at the solid–liquid interface.

CRediT authorship contribution statement

Dejian Zhang: Investigation, Methodology, Data curation, Formal analysis, Writing - original draft. **Satoko Takase:** Methodology, Writing - review & editing. **Gyoko Nagayama:** Conceptualization, Methodology, Supervision, Writing - review & editing.

Declaration of Competing Interest

The authors declare no competing financial interest or personal relationships that could have appeared to influence the work reported in this paper.

Acknowledgements

This work is supported by the Ministry of Education, Science and Culture of the Japanese Government through the Grant-in Aid for Scientific Research, Project No. 18H01385 and No. 21360099, "Nanotechnology Platform Program", Grant Number JPMXP09 F20YA0001 & F20FA0017, and the Initiative for Realizing Diversity in the Research Environment by Ministry of Education, Culture, Sports, Science and Technology, Japan. Mr. Taiki Maeda and Mr. Naoki Shiraishi are acknowledged for their assistance to fabricate the samples.

References

[1] M. Liu, S. Wang, L. Jiang, Nature-inspired superwettability systems. Nat. Rev. Mater. 2 (2017) 1–17.

[2] S. Wang, K. Liu, X. Yao, L. Jiang, Bioinspired surfaces with superwettability: new insight on theory, design, and applications. Chem. Rev. 115 (2015) 8230–8293.

[3] Z. Han, X. Feng, Z. Guo, S. Niu, L. Ren, Flourishing bioinspired antifogging materials with superwettability: progresses and challenges. Adv. Mater. 30 (2018) 1704652.

[4] A. Askounis, K. Sefiane, V. Koutsos, M.E. Shanahan, Effect of particle geometry on triple line motion of nano-fluid drops and deposit nano-structuring. Adv. Colloid Interface Sci. 222 (2015) 44–57.

[5] Y. Tian, B. Su, L. Jiang, Interfacial material system exhibiting superwettability. Adv. Mater. 26 (2014) 6872–6897.

[6] J. Wang, W. Gao, H. Zhang, M. Zou, Y. Chen, Y. Zhao, Programmable wettability on photocontrolled graphene film. Sci. Adv. 4 (2018) eaat7392.

[7] S.H. Sajadinia, F. Sharif, Thermodynamic analysis of the wetting behavior of dual scale patterned hydrophobic surfaces. J. Colloid Interface Sci. 344 (2010) 575–583.

[8] A. Marmur, S. Kojevnikova, Super-hydrophobic surfaces: Methodological considerations for physical design. J. Colloid Interface Sci. 568 (2020) 148–154.

[9] D. Chandler, Interfaces and the driving force of hydrophobic assembly. Nature 437 (2005) 640–647.

[10] A. Poynor, L. Hong, I. K. Robinson, S. Granick, Z. Zhang, P. A. Fenter, How water meets a hydrophobic surface. Phys. Rev. Lett. 97 (2006) 266101.

[11] L. Hu, S. Zhang, Y. Zhang, B. Li, A flexible nanofiber-based membrane with superhydrophobic pinning properties. J. Colloid Interface Sci. 472 (2016) 167–172.

[12] F. Chu, X. Wu, L. Wang, Meltwater evolution during defrosting on superhydrophobic surfaces. ACS Appl. Mater. Interfaces 10 (2018) 1415–1421.

[13] Y. Kita, C.M. Dover, A. Askounis, Y. Takata, K. Sefiane, Drop mobility on superhydrophobic microstructured surfaces with wettability contrasts. Soft matter 14 (2018) 9418–9424.

[14] R.N. Wenzel, Resistance of Solid Surfaces to Wetting by Water. Ind. Eng. Chem. Res. 28 (1936) 988–994.

[15] A.B.D. Cassie, S. Baxter, Wettability of Porous Surfaces. Trans. Faraday Soc. 40 (1944) 546–551.

[16] M. Miwa, A. Nakajima, A. Fujishima, K. Hashimoto, T. Watanabe, Effects of the surface roughness on sliding angles of water droplets on superhydrophobic surfaces. Langmuir 16 (2000) 5754–5760.

[17] A. Marmur, Wetting on hydrophobic rough surfaces: to be heterogeneous or not to be?. Langmuir 19 (2003) 8343–8348.

[18] E. Bormashenko, Progress in understanding wetting transitions on rough surfaces. Adv. Colloid Interface Sci. 222 (2015) 92–103.

[19] J. Yang, J. Wang, C.W. Wang, X. He, Y. Li, J.B. Chen, F. Zhou, Intermediate wetting states on nanoporous structures of anodic aluminum oxide surfaces. Thin Solid Films 562 (2014) 353–360.

[20] H.Y. Erbil, C.E. Cansoy, Range of applicability of the Wenzel and Cassie−Baxter equations for superhydrophobic surfaces. Langmuir 25 (2009) 14135–14145.

[21] G. Nagayama, D. Zhang, Intermediate wetting state at nano/microstructured surfaces. Soft Matter 16 (2020) 3514–3521.

[22] D. Surblys, Y. Kawagoe, M. Shibahara, T. Ohara, Molecular dynamics investigation of surface roughness scale effect on interfacial thermal conductance at solid–liquid interfaces. J. Chem. Phys. 150 (2019) 114705.

[23] Y. Chen, C. Zhang, Role of surface roughness on thermal conductance at liquid–solid interfaces. Int. J. Heat Mass Transf. 78 (2014) 624–629.

[24] G. Nagayama, M. Kawagoe, A. Tokunaga, T. Tsuruta, On the evaporation rate of ultra-thin liquid film at the nanostructured surface: a molecular dynamics study. Int. J. Therm. Sci. 49 (2010) 59–66.

[25] P. Papadopoulos, L. Mammen, X. Deng, D. Vollmer, H.J. Butt, How superhydrophobicity breaks down. Proc. Natl. Acad. Sci. 110 (2013) 3254–3258.

[26] D. Daniel, J.V. Timonen, R. Li, S.J. Velling, J. Aizenberg, Oleoplaning droplets on lubricated surfaces. Nat. Phys. 13 (2017) 1020–1025.

[27] R. Poetes, K. Holtzmann, K. Franze, U. Steiner, Metastable underwater superhydrophobicity. Phys. Rev. Lett. 105 (2010) 166104.

[28] G. Manukyan, J.M. Oh, D. Van Den Ende, R.G. Lammertink, F. Mugele, Electrical switching of wetting states on superhydrophobic surfaces: a route towards reversible Cassie-to-Wenzel transitions. Phys. Rev. Lett. 106 (2011) 014501.

[29] H. Rathgen, F. Mugele, Microscopic shape and contact angle measurement at a superhydrophobic surface. Faraday Discuss. 146 (2010) 49–56.

[30] M. Sakai, T. Yanagisawa, A. Nakajima, Y. Kameshima, K. Okada, Effect of surface structure on the sustainability of an air layer on superhydrophobic coatings in a water−ethanol mixture. Langmuir 25 (2009) 13–16.

[31] M.S. Bobji, S.V. Kumar, A. Asthana, R.N. Govardhan, Underwater sustainability of the “Cassie” state of wetting. Langmuir 25 (2009) 12120–12126.

[32] P. Wang, J. Su, M. Shen, M. Ruths, H. Sun, Detection of liquid penetration of a micropillar surface using the quartz crystal microbalance. Langmuir 33 (2017) 638–644.

[33] A. Checco, B.M. Ocko, A. Rahman, C.T. Black, M. Tasinkevych, A. Giacomello, S. Dietrich, Collapse and reversibility of the superhydrophobic state on nanotextured surfaces. Phys. Rev. Lett. 112 (2014) 216101.

[34] N. Saad, R. Dufour, P. Campistron, G.Nassar, J. Carlier, M. Harnois, B. Merheb, R. Boukherroub, V. Senez, J. Gao, V. Thomy, Characterization of the state of a droplet on a micro-textured silicon wafer using ultrasound. J. Appl. Phys. 112 (2012) 104908.

[35] S. Li, S. Lamant, J. Carlier, M. Toubal, P. Campistron, X. Xu, G.Vereecke, V. Senez, V. Thomy, B. Nongaillard, High-frequency acoustic for nanostructure wetting characterization. Langmuir 30 (2014) 7601–7608.

[36] R. Dufour, N. Saad, J. Carlier, P. Campistron, G. Nassar, M. Toubal, R. Boukherroub, V. Senez, B. Nongaillard, V. Thomy, Acoustic tracking of Cassie to Wenzel wetting transitions. Langmuir 29 (2013) 13129–13134.

[37] J.C. Tuberquia, W.S. Song, G.K. Jennings, Investigating the superhydrophobic behavior for underwater surfaces using impedance-based methods. Anal. Chem. 83 (2011) 6184–6190.

[38] D. Zhang, G. Nagayama, Effective Wetting Area Based on Electrochemical Impedance Analysis: Hydrophilic Structured Surface. Langmuir 35 (2019) 16508–16513.

[39] M.W. Yang, S.Y. Lin, A method for correcting the contact angle from the $\theta/2$ method. Colloids Surf. A 220 (2003) 199–210.

[40] B. Yeum, ZSimpWin Version 2.00. *Echem Software Ann Arbor* (2001), MI, USA.

[41] T. Young, An essay on the cohesion of fluids. Philosophical transactions of the royal society of London 95 (1805) 65–87.

[42] K. Foroutan-pour, P. Dutilleul, D.L. Smith, Advances in the implementation of the box-counting method of fractal dimension estimation. Appl. Math. Comput. 105 (1999) 195–210.

[43] H. Sasaki, Fractal Analysis System Version 3.4.7. *The National Agriculture and Food Research Organization* (2006), Tochigi, Japan.

[44] W.P. Gomes, D. Vanmaekelbergh, Impedance spectroscopy at semiconductor electrodes: review and recent developments. Electrochim. Acta 41 (1996) 967–973.

[45] A. Hankin, F.E. Bedoya-Lora, J.C. Alexander, A. Regoutz, G.H. Kelsall, Flat band potential determination: avoiding the pitfalls. J. Mater. Chem. A 7 (2019) 26162–26176.

[46] J. Kuang, Z. Ba, Z. Li, Z. Wang, J. Qiu, The study on corrosion resistance of superhydrophobic coatings on magnesium. Appl. Surf. Sci. 501 (2020) 144137.

[47] Y. Zou, Y. Wang, S. Xu, T. Jin, D. Wei, J. Ouyang, D. Jia, Y. Zhou, Superhydrophobic

double-layer coating for efficient heat dissipation and corrosion protection. Chem. Eng. J. 362 (2019) 638–649.

[48] B. Díaz, E. Härkönen, J. Światowska, V. Maurice, A. Seyeux, P. Marcus, M. Ritala, Low-temperature atomic layer deposition of Al_2O_3 thin coatings for corrosion protection of steel: Surface and electrochemical analysis. Corros. Sci. 53 (2011) 2168–2175.